processes

MDPI

Article

Effects of Dual-Auger Composite Borehole Placement on Upper-Corner Methane Control: Numerical Modeling and Field Monitoring

Zhipeng Che [1,2], Xinghua Zhang [1,2], Xiaoguang Qiao [1,2], Lulu Zhang [1,2,*], Xiaobo Lv [1,2], Jintang Song [1,2] and Wenjun Li [1,2]

[1] School of Safety and Emergency Management Engineering, Taiyuan University of Technology, Jinzhong 030600, China; 2024511312@link.tyut.edu.cn (Z.C.); zhangxinghua@tyut.edu.cn (X.Z.); qiaoxiaoguang@tyut.edu.cn (X.Q.); lvxiaobo@tyut.edu.cn (X.L.); 2024521910@link.tyut.edu.cn (J.S.); liwenjun2074@link.tyut.edu.cn (W.L.)
[2] Shanxi Key Laboratory of Life Rescue Access Construction Technology and Equipment for Confined Space Emergency Response, Taiyuan University of Technology, Taiyuan 030024, China
* Correspondence: zhanglulu@tyut.edu.cn; Tel.: +86-18118762524

Abstract

Methane (CH_4) migration from the goaf can cause accumulation in the upper corner of U-ventilated working faces. Composite-borehole placement and methane control were investigated at working face 81506 of Huayang No. 2 Mine. A heterogeneous porous-medium model was developed in Ansys Fluent using user-defined functions (UDFs) to describe spatially varying porosity and flow resistance. Five borehole-to-corner distances (10, 20, 30, 40, and 50 m) were evaluated. A composite borehole was constructed by coordinated dual-auger drilling at the selected distance of 40 m, followed by 60 days of field monitoring. At 40 m, simulated mean and maximum upper-corner CH_4 concentrations were 0.2475% and 0.8659%, respectively, and mixed-gas mass flow from the goaf toward the working face decreased by 47.77% relative to the no-drainage case. At 50 m, the maximum concentration exceeded 1.0%, making 40 m the largest tested distance meeting this criterion. In the field, mean and maximum upper-corner CH_4 concentrations decreased by 48.43% and 39.73%, respectively, to 0.557% and 0.88%. Composite-borehole drainage was thus effective under the tested conditions, with local maximum concentration serving as a key placement criterion.

Keywords: goaf; upper-corner methane; dual-auger composite borehole; coordinated dual-auger drilling; numerical simulation; field monitoring

Check for updates

Academic Editor: Iván García Kerdan

Received: 16 October 2026
Revised: 6 November 2026
Accepted: 16 November 2026
Published: 18 November 2026

Copyright: © 2026 by the authors. Licensee MDPI, Basel, Switzerland. This article is an open access article distributed under the terms and conditions of the Creative Commons Attribution (CC BY) license.

1. Introduction

During mining, methane (CH_4) released from the coal seam and surrounding coal and rock enters the goaf, which becomes a major methane source for the working face [1–3]. Methane is transported from the goaf to the working face by ventilation and air leakage. Working-face methane concentrations and the risk of local accumulation are influenced by emission rates and migration pathways [4–6]. Control of goaf methane sources and migration toward high-risk working-face areas is therefore central to methane management in high-gas mines.

At working faces with U-type ventilation, the upper corner is particularly susceptible to methane accumulation from the goaf. Substantial spatial heterogeneity in goaf porosity and permeability is produced by roof fracturing, collapse, and compaction. Relatively

permeable pathways for air leakage and methane migration may be formed by fractures near the working face and along the goaf margins [4–6]. Methane release from the goaf to the working face is further governed by differences in compaction and flow resistance [7,8]. The upper corner is located adjacent to the goaf, where working-face airflow meets the return airway. Methane may consequently be transported toward the return-air side, where it may accumulate under the effects of air leakage, buoyancy, and local low-velocity recirculation. Upper-corner methane accumulation may not be eliminated by increasing ventilation alone. Air leakage into the goaf may be increased by excessive pressure differences, which may also alter methane migration pathways. Methane control should therefore include management of goaf sources and migration pathways alongside local dilution.

In interconnected goafs, leakage pathways have been identified through tracer tests, and numerical models have been used to evaluate the combined effects of working-face ventilation and gas extraction through a high-level drainage roadway on upper-corner methane [9].

Existing measures for upper-corner and goaf methane control can be classified into three categories according to their mechanisms. The first category comprises ventilation and local flow control. Local methane concentrations can be rapidly reduced by adjusting airflow rates or adopting U-, Y-, or W-type ventilation. Methane is diluted and airflow is redistributed by these measures. However, persistent methane sources deep in the goaf are only partly controlled, and air leakage may be increased [2,10,11]. In the second category, methane is diverted from a wider area of the goaf through dedicated routes, including high- and low-level drainage roadways, tailgate roadways, and buried or inserted pipes. Drainage performance is influenced by inlet location, spacing, suction pressure, and pipeline integrity. Dedicated roadways are also constrained by construction time, maintenance requirements, and available space [12–14]. The third category comprises surface vertical boreholes, roof or adjacent-seam boreholes, long-reach directional boreholes, and other underground boreholes. Suction-driven flow is established through these boreholes, thereby altering goaf pressure fields and methane migration pathways [15–17]. The applicability of each measure depends on site conditions. Borehole drainage allows relatively flexible placement. Further development is warranted where construction adaptability and interception of methane near its source are required.

Air curtains have also been assessed through boundary-layer analysis, Fluent simulations, and field measurements to determine their effects on goaf air leakage and upper-corner gas concentration [18].

Goaf methane control by borehole drainage is influenced by borehole geometry and placement. Drainage coverage has been increased by optimizing borehole positions, numbers, and layouts [19,20]. Spatial coverage can be extended using large-diameter and long-reach directional boreholes [17,20]. Cross-measure, tree-type, and branched boreholes have been used in different strata and complex coal and rock conditions [21–23]. However, conventional placement parameters and individual borehole configurations have received most attention. The combined effects of borehole geometry, position, and methane transport in the goaf remain insufficiently understood.

For conventional large-diameter boreholes, hole spacing and the first borehole's distance from the upper corner have been evaluated using Fluent simulations and field tests [24]. Long horizontal boreholes have been studied through analyses of effective drainage range and borehole interaction [25]. High-level layouts have been investigated using fracture-development and gas-flow analyses [26], and pressure-relief gas extraction has been designed to follow the evolution and zoning of overburden permeability [27].

Previous research has focused mainly on conventional single, independent multiple, directional, and branched boreholes. Drainage through continuous, noncircular compos-

ite boreholes with large cross-sections and its effects on methane transport in heterogeneous goafs remain less well understood. For upper-corner methane control, the effects of composite-borehole location on pressure, air leakage, and methane transport require further investigation. The stability of drainage performance over time must also be assessed. Numerical analysis of the mechanisms must therefore be combined with continuous field monitoring. The novelty here is the use of coordinated dual-auger drilling to form a continuous, large-cross-section composite borehole in a single pass, which increases the drainage cross-section per borehole and reduces the number of boreholes required for a given coverage compared with conventional large-diameter or multiple independent boreholes.

Upper-corner methane control was investigated using large-diameter composite boreholes formed by coordinated dual-auger drilling at working face 81506 of Huayang No. 2 Mine. A heterogeneous model of goaf methane transport was developed in Ansys Fluent. Pressure, velocity, and CH_4 distributions were examined at different borehole-to-corner spacings. The selected layout and its effectiveness in controlling upper-corner methane were then assessed through field drilling and 60 days of continuous drainage monitoring.

2. Numerical Model and Methods

Simulations were performed using Ansys Fluent 2024 R2, and post-processing was conducted using Tecplot 2024 R1 and Origin 2024.

2.1. Geometry and Assumptions

A three-dimensional computational domain was constructed for fully mechanized working face 81506 at Huayang No. 2 Mine. The goaf dimensions were 200 m along strike, 200 m along dip, and 4 m vertically. The intake and return airway cross-sections were both 4 m × 4 m; the working-face passage was 4 m wide. The x-axis was defined along dip, with x = 0 on the return-air side and x = 200 m on the intake-air side. The z-axis was defined along strike, with z = 0 at the working-face–goaf interface and negative z directed into the goaf. The y-axis was vertical. The borehole was positioned on the return-air side and represented as two communicating circular holes, each 550 mm in diameter, separated by a 70 mm gap, giving an overall width of 1170 mm. The borehole interior was treated as a free-flow region without additional porous resistance. The geometric model and borehole cross-section are shown in Figure 1a,b, respectively.

The following assumptions were adopted to simplify the calculations:

(1) Goaf flow was assumed to be steady, and transient effects of working-face advance were neglected.
(2) Caved rock and residual coal were represented as a continuous, isotropic porous medium. Spatial porosity variation was represented by a continuous function based on the O-ring theory of mining-induced fractures.
(3) The gas mixture was treated as an ideal gas. Heat release from methane oxidation and spontaneous combustion of residual coal was excluded.
(4) Time-dependent deformation of the surrounding rock and compaction of the goaf were neglected. The porosity field was represented by an empirical distribution for the final compacted state.

2.2. Governing Equations and Heterogeneous Porous-Medium Model

2.2.1. Governing Equations

After extraction, spatial heterogeneity in caved-rock porosity and permeability is produced by mining-induced damage, boundary constraints, and prolonged compaction. Under the O-ring theory of mining-induced fractures [2], relatively high porosity and per-

meability are associated with well-developed fractures near the working face and along both dip-direction margins. Both properties are reduced by compaction deeper in the goaf. Local porosity, permeability, and viscous and inertial resistance coefficients were calculated from cell-centroid coordinates using user-defined functions (UDFs). The resulting properties were assigned to the goaf porous-medium zone. Abrupt property changes at discrete zone boundaries are avoided by this continuous formulation. The permeable face-side region, marginal fracture pathways, and compacted interior are represented continuously.

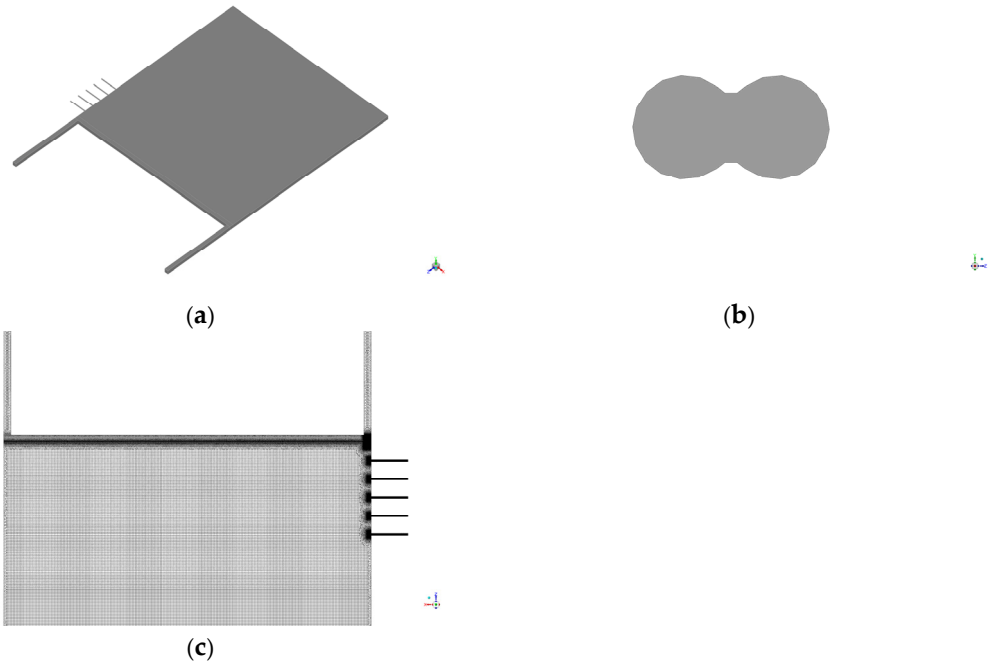


Figure 1. Geometry and computational mesh of the goaf methane drainage model: (**a**) computational domain; (**b**) composite-borehole cross-section; (**c**) mesh distribution on the horizontal plane at y = 2 m.

A layered goaf model implemented in Ansys Fluent has linked gas migration to vertical and marginal variations in porosity and permeability [28]. Under double roof cutting and Y-type ventilation, spatial property functions have also been assigned through Fluent user-defined functions to compare combined borehole and roadway drainage [29]. These studies support accounting for spatial heterogeneity; the empirical functions used in the present model are specified in Equations (5)–(8).

Mixture flow was described by the Reynolds-averaged Navier–Stokes equations. The advection and diffusion of CH_4, oxygen (O_2), and nitrogen (N_2) were calculated using species transport. N_2 was specified as the balance species. The continuity, momentum, and species-transport equations are given below.

Continuity equation:

$$\frac{\partial \rho}{\partial t} + \nabla \cdot (\rho \vec{v}) = S_m \tag{1}$$

Here, ρ is the mixture density, $\vec{v}$ is the velocity vector, and S_m is the volumetric total-mass source term. During the stage without a methane source, $S_m = 0$. The momentum equation is:

$$\frac{\partial (\rho \vec{v})}{\partial t} + \nabla \cdot (\rho \vec{v} \vec{v}) = -\nabla \mathrm{p} + \nabla \cdot [\mu_{eff} (\nabla \vec{v} + \nabla \vec{v}^{\,T})] + \rho \vec{g} + S_p \tag{2}$$

Here, μ_{eff} is the sum of molecular and turbulent viscosities, $\vec{g}$ is gravitational acceleration, and S_p is the porous-medium resistance term in the momentum equation. The transport equation for species i is:

$$\frac{\partial(\rho Y_i)}{\partial t} + \nabla \cdot (\rho \vec{v} Y_i) = -\nabla \cdot \vec{J}_i + S_i \tag{3}$$

Here, Y_i is the species mass fraction, $\vec{J}_i$ is the diffusive flux, and S_i is the species source term. Equal values were assigned to the CH_4 source and the total-mass source in the continuity equation. All other species source terms were set to zero. The simplified energy equation is:

$$\frac{\partial(\rho E)}{\partial t} + \nabla \cdot [\vec{v}(\rho \mathrm{E} + \mathrm{p})] = \nabla \cdot (k_{eff} \nabla T + \tau_{eff} \cdot \vec{v}) + S_E \tag{4}$$

Here, E is total energy, k_{eff} is effective thermal conductivity, and τ_{eff} is the effective stress tensor. The energy equation was solved to describe convective and conductive energy transport in the gas mixture. The calculated temperature was used in the ideal-gas density relation and could therefore influence the airflow field and methane transport indirectly. Methane oxidation and spontaneous combustion of residual coal were excluded, and no corresponding reaction heat sources were imposed. Coupling between the mass source and the energy equation was handled by the solver. The contribution of species diffusion to energy transport was disabled. Turbulence was modeled using the SST k-ω model because it resolves the near-wall region without wall functions and is well suited to the refined meshes and shear layers near the airway, working-face, and borehole walls, while remaining robust in the far field through its blending function.

2.2.2. User-Defined Functions for Porous-Medium Properties and Methane Sources

For cell-centroid coordinates (m), d = −z and s = min(x, 200 − x) measure depth behind the face and distance to the nearer side boundary, respectively:

$$\begin{gathered} I_f = \exp\left[-\tfrac{1}{2}\left(\tfrac{d}{35}\right)^2\right], \\ I_s = \exp\left[-\tfrac{1}{2}\left(\tfrac{s}{25}\right)^2\right]\exp\left[-\tfrac{d}{120}\right] \\ I_d = \frac{1}{1+\exp\left[-\frac{(d-145)}{18}\right]}, \\ I_c = \exp\left[-\tfrac{1}{2}\left[\left(\tfrac{(x-100)}{45}\right)^2 + \left(\tfrac{(z+160)}{28}\right)^2\right]\right] \end{gathered} \tag{5}$$

The porosity bounds in the model were constrained by the bulking factor of the roof strata. Using $n = 1 - 1/K_p$, an initial bulking factor of 1.5~1.8 for sandstone-dominated roof gives n ≈ 0.33~0.44, and a residual bulking factor of 1.03~1.10 after compaction gives n ≈ 0.03~0.09; the adopted limits of 0.072 and 0.44 and the base value of 0.20 are consistent with these ranges. The characteristic lengths (35, 25, 120, 145, 18, 45, and 28 m) describe the spatial attenuation of porosity and were set according to the 200 m goaf extent and the general roof-collapse and compaction zoning at the site, consistent with the attenuation ranges reported for longwall goafs [28,29]. These indices modulate the porosity and the porous resistance, with the viscous and inertial resistances derived from porosity through Ergun-type relations. The resulting fields were checked indirectly against the measured gas emission and the field CH_4 concentration at 40 m.

The fracture and compaction indices are combined as:

$$I_r = 1 - \left(1 - I_f\right)(1 - I_s), \quad I_{comp} = 1 - (1 - I_d)(1 - I_c) \tag{6}$$

Porosity is calculated with fracture, compaction, and vertical corrections:

$$n = \mathrm{clip}\left\{\left[0.15 + 0.25 I_r (1 - 0.90 I_d) - 0.07 I_{\mathrm{comp}}\right]\left[0.90 + 0.20\frac{y}{4}\right], 0.072, 0.44\right\} \tag{7}$$

Here, n is porosity. Spatial scales, porosity coefficients, and clipping bounds are empirical inputs.

The equivalent particle diameter and Ergun resistance coefficients are:

$$d_p = 0.10\left(\frac{0.23}{0.10}\right)^{\frac{n-0.072}{0.44-0.072}}$$
$$\frac{1}{K} = \frac{[150(1-n)^2]}{d_p^2 n^3}, \quad C_2 = \frac{[3.5(1-n)]}{d_p n^3} \tag{8}$$

The empirical particle-diameter range is 0.10–0.23 m. Identical directional resistances are bounded within 10–10^7 m^{-2} (viscous) and 0.1–1.5 × 10^4 m^{-1} (inertial).

The functions apply equal, time-independent volumetric sources (kg m^{-3} s^{-1}) to continuity and CH_4 transport inside the goaf. Release decreases with depth and height. The full-domain integral is 0.2616 kg s^{-1}, equivalent to 6.54 × 10^{-6} kg m^{-2} s^{-1} over the floor.

Methane source term was derived from the gas emission report of Huayang No. 2 Mine for working face 81506. The report provides the measured ventilation air volume, return-air CH_4 concentration, and gas drainage volume during the monitoring period. Using a mass balance on the working face, the steady goaf CH_4 emission rate was estimated as 0.2616 kg/s. This value represents the average emission level during the field monitoring period rather than transient fluctuations. The same total source strength was applied in all numerical cases. Its spatial distribution was prescribed by weighting the source in each goaf cell with the same fracture/compaction heterogeneity indices used for porosity and flow resistance, i.e., Equations (5)–(8), and then normalizing the cell sources so that their volume integral equals 0.2616 kg/s.

2.3. Boundary Conditions and Simulation Cases

A pressure-based solver was used. Stages 1 and 2 were solved in steady mode using the semi-implicit method for pressure-linked equation (SIMPLE) pressure–velocity coupling. Stage 3 was solved in transient mode using pressure-implicit with splitting of operator (PISO) coupling. The main boundary conditions are listed in Table 1.

Table 1. Main boundary conditions.

Boundary	Type	Parameters
Intake airway inlet	Velocity-inlet	Air velocity: 2.5 m/s; O_2 mass fraction: 0.23
Return airway outlet	Pressure outlet	Pressure 0 Pa
Gas source	UDF-defined volumetric mass source	$q_{CH4} = 6.54 \times 10^{-6}$ kg/(m²·s)
Borehole outlet	Pressure outlet	−1200 Pa

For the spacing comparison, only the borehole-to-corner spacing was varied to assess its effect on methane control. Borehole geometry and length, suction pressure, intake velocity, and floor methane emission were held constant. The spacing, L_d, was set to 10, 20, 30, 40, and 50 m. All remaining geometric parameters and boundary conditions were held constant across cases.

The calculations were performed in three consecutive stages. Between stages, the preceding solution was carried forward without reinitialization.

(1) The ventilation field was established in Stage 1. The porous-medium UDFs were retained, the total-mass and CH_4 source terms were disabled, and the borehole outlet was specified as a wall. After hybrid initialization, the temperature was set to 293.15 K, and the species mass fractions were patched to $CH_4 = 0$ and $O_2 = 0.23$; CO_2 and H_2O were neglected.

(2) The methane field without drainage was established in Stage 2. The borehole outlet was retained as a wall, and the methane source was activated. Stage 3 was initiated after the flow and methane fields had stabilized.
(3) The methane field with drainage was established in Stage 3. The CH_4 source was retained, and the borehole outlet was changed to a pressure outlet at a gauge pressure of −1200 Pa. The calculation was continued until the reported stable state was reached.

2.4. Numerical Sensitivity

2.4.1. Mesh Sensitivity

The computational mesh was generated using the Poly-Hexcore method in Fluent Meshing and locally refined for each region. The characteristic cell sizes were 0.64 m in the goaf, 0.32 m in the working-face passage and airways, and 0.16 m in the borehole. A wall mesh size of 0.08 m was used at the borehole, and the upper-corner cell size was reduced to 0.16 m using a body of influence. The global minimum cell size was 0.04 m, and the mesh growth rate was 1.20. The final mesh comprised 1,315,978 cells. The local mesh and local borehole refinement are shown in Figure 1c.

Coarse, medium, and fine meshes were generated to assess mesh sensitivity. Geometry, local refinement regions, and boundary-layer settings were held constant. The main mesh parameters are listed in Table 2.

Table 2. Mesh sensitivity results.

Mesh Scheme	Cell Count	Maximum CH_4 Concentration (%)	Borehole CH_4 Mass Flow (kg/s)	CH_4 Concentration Deviation	CH_4 Flow Deviation
Coarse mesh	505,393	0.8573	0.2894	1.7%	2.4%
Medium mesh	1,315,978	0.8659	0.2916	0.8%	1.7%
Fine mesh	2,139,503	0.8725	0.2965	—	—

For the 40 m spacing, the maximum upper-corner CH_4 concentration and borehole CH_4 mass flow rate were compared across the three meshes. Differences of less than 3% were obtained between the medium and fine meshes for both metrics, indicating limited sensitivity to further refinement. The medium mesh was therefore used in subsequent simulations.

2.4.2. Transient Settings and Time-Step Sensitivity

Drainage time is measured from opening the borehole outlet (t = 0). Each run starts from the corresponding Stage 2 solution. The step size and maximum iterations per step are 0.1 s and 10. Durations for the 10, 20, 30, 40, and 50 m cases are 200 s. Physical stabilization is assessed separately over 100–200 s using 3%.

Time-step sensitivity was assessed by comparing $\Delta t/2$(0.05 s), Δt(0.1 s), and $2\Delta t$(0.2 s) at L_d = 40 and 50 m. Each run was initialized from the identical Stage 2 solution and compared at matched physical times. The results are summarized in Table 3. For each time step, the calculation was advanced from $t = 0$ (borehole outlet opened) to 200 s. At each time step, up to 10 iterations were performed, and convergence was judged from the scaled residuals of continuity, momentum, species, and energy, all of which were required to fall below 10^{-4} before advancing. Physical stabilization was assessed independently over t = 100–200 s: the area-weighted mean and maximum upper-corner CH_4 concentrations and the borehole CH_4 mass flow were monitored, and the solution was regarded as stable when the relative changes in these quantities over the 100 s window remained below 3%. All cases satisfied this criterion at t = 200 s. As shown in Table 3, the maximum relative differences between $\Delta t/2$ and Δt were 1.34% (40 m) and 1.35% (50 m), and those between Δt and $2\Delta t$ were 2.30% (40 m) and 2.77% (50 m). More importantly, the classification against

the 1.0% screening value was unchanged: the 40 m case remained below 1.0% and the 50 m case remained above 1.0% for all three time steps. A time step of $\Delta t = 0.1$ s was therefore adopted for all simulations, as it provides a satisfactory balance between accuracy and computational cost.

Table 3. Time-step sensitivity at 40 and 50 m.

L_d (m)	Step Level	Time Step (s)	$C_{A,avg}$ (vol.%)	$C_{A,max}$ (vol.%)	$\dot{m}_{CH4}$ (kg s^{-1})	Maximum Relative Error
40	Δt	0.1	0.2475	0.8659	0.2916	–
40	Δt/2	0.05	0.2449	0.8543	0.2933	1.34%
40	2Δt	0.2	0.2418	0.8558	0.2884	2.30%
50	Δt	0.1	0.2699	1.0577	0.2707	–
50	Δt/2	0.05	0.2668	1.0434	0.2683	1.35%
50	2Δt	0.2	0.2754	1.0703	0.2782	2.77%

Simulation omits overlying strata effects, dynamic mining-induced fractures, atmospheric pressure fluctuations, and operational variations, and evaluates concentrations on an area-weighted plane at y = 2 m from the stabilized transient state.

The net mass imbalance over the computational domain was below 0.5% of the inlet mass flow in all reported cases. Because the species equation is linear in the source term under a fixed flow field, the upper-corner concentration scales approximately with source strength. The 40 m case therefore remains below 1.0% for source increases up to about 15%, and the 50 m case remains above 1.0%. The 40 m recommendation is thus valid for the reported emission rate and moderate variations.

3. Effects of Borehole Placement on Methane Migration in the Goaf

3.1. Baseline Conditions Without Drainage

The Stage 2 solution, with the methane source active and the borehole outlet closed, was used as the baseline for upper-corner methane accumulation. The velocity distribution on the horizontal plane at y = 2 m is shown in Figure 2a. The main ventilation route comprised the working-face passage and the intake and return airways, where velocities were substantially higher than in the goaf. Gas movement deep in the goaf was limited by porous-medium resistance, and dilution by ventilation was weak. Elevated methane concentrations could therefore develop under continuous methane release.

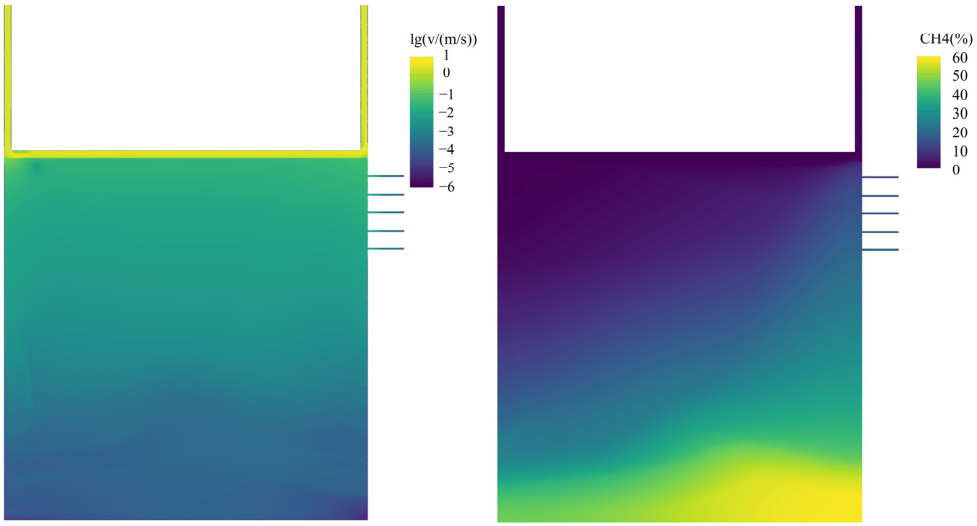
The CH_4 distribution on the horizontal plane at y = 2 m is shown in Figure 2b. Methane concentrations generally increased with distance from the working face and were asymmetric along the dip direction. Higher concentrations occurred mainly near the goaf interface and generally decreased toward the working-face passage, producing a marked gradient across the monitoring plane.

A fixed upper-corner monitoring plane was defined at y = 2 m over x = 0–4 m and z = 0–4 m. Without drainage, the area-weighted mean CH_4 concentration on this plane was 1.2719%, and the maximum face-element concentration was 2.1028%. The area-weighted mean CH_4 concentration at the return-air outlet was 0.9785%. This case was used as the reference for subsequent comparisons, with the monitoring areas and statistical methods held constant. Drainage performance was evaluated using the mean and maximum concentrations and changes in the high-concentration region.

3.2. Selection of Borehole Spacing

Boreholes located 10, 20, 30, 40, and 50 m along strike from the upper corner were compared using the final saved solution for each case. Borehole geometry and length, intake velocity, and floor methane emission were held constant across the cases. A CH_4 alarm

threshold of ≥1.0% for the return-air corner sensor is specified in the Coal Mine Safety Regulations. A maximum upper-corner CH_4 concentration below 1.0% was therefore used as the primary screening criterion. Mean concentration and borehole drainage metrics were considered as supplementary indicators.



(**a**) (**b**)

Figure 2. Baseline flow and methane distributions without drainage: (**a**) velocity contours at y = 2 m; (**b**) methane (CH_4) contours at y = 2 m.

The CH_4 distributions at y = 2 m for the different spacings are shown in Figure 3. Mean and maximum concentrations were calculated on the same monitoring plane for all cases to compare overall concentrations and local accumulation.

The reported steady-state results for the different spacings are summarized in Table 4. The mean and maximum upper-corner CH_4 concentrations as functions of L_d are shown in Figure 4a. Upper-corner methane control efficiency was defined as the relative reduction in mean concentration:

$$\eta_{uc} = \frac{C_0 - C_{L_d}}{C_0} \times 100\% \quad (9)$$

Here, C_0 denotes the area-weighted mean CH_4 concentration on the upper-corner monitoring plane without drainage, and C_{Ld} denotes the corresponding value for spacing L_d in the final saved solution.

Table 4. Reported steady-state results for different borehole spacings.

L_d (m)	Mean Upper-Corner CH_4 (%)	Maximum Upper-Corner CH_4 (%)	CH_4 Mass Flow (kg/s)	Mixed-Gas Mass Flow (kg/s)	Outlet CH_4 (%)
No extraction	1.2719	2.1028	—	—	—
10	0.1483	0.4428	0.2516	7.1948	6.0527
20	0.1892	0.5716	0.3444	6.7951	8.6817
30	0.2175	0.7578	0.2669	5.5582	8.2482
40	0.2475	0.8659	0.2916	5.1245	9.7009
50	0.2699	1.0577	0.2707	4.6006	10.0231

At L_d = 40 m, the mean upper-corner CH_4 concentration was reduced from 1.2719% without drainage to 0.2475%, and the maximum was reduced from 2.1028% to 0.8659%. The relative reductions in mean and maximum concentration were 80.54% and 58.82%, respectively. The CH_4 and total mixed-gas mass flow rates at the borehole outlet were

0.2916 and 5.1245 kg/s, respectively. The reported mass-weighted outlet CH_4 concentration was 9.7009%.

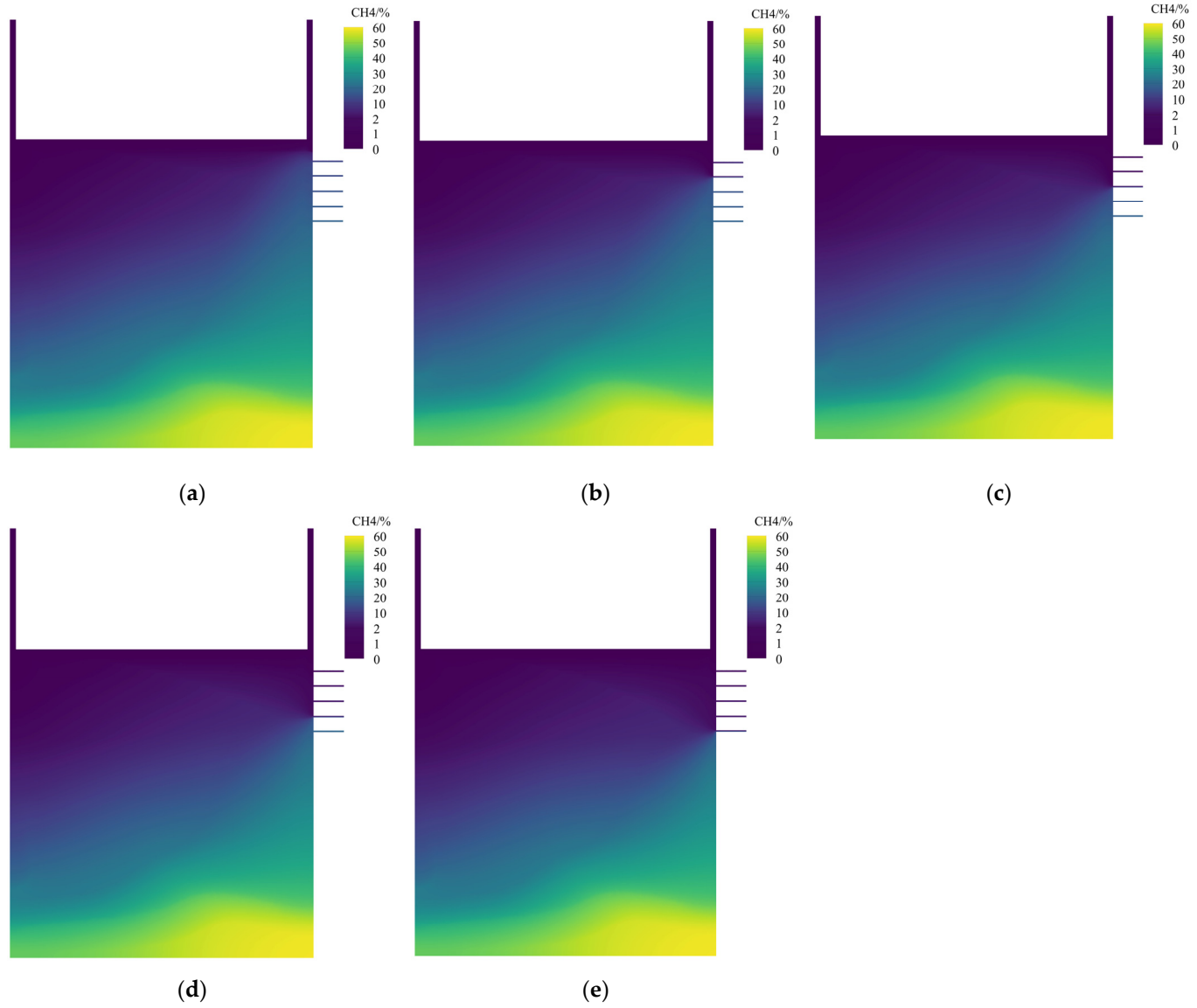


Figure 3. Methane (CH_4) distributions at y = 2 m for different borehole-to-corner spacings: (**a**) Ld = 10 m; (**b**) 20 m; (**c**) 30 m; (**d**) 40 m; (**e**) 50 m.

At L_d = 50 m, the mean and maximum upper-corner CH_4 concentrations were 0.2699% and 1.0577%, respectively. Although the mean was below 1.0%, the local maximum exceeded the threshold. Local methane accumulation was therefore not adequately characterized by the mean alone. The final maximum concentrations were below 1.0% for all cases from 10 to 40 m. The lowest concentration was obtained at 10 m, whereas 40 m was the largest tested spacing that met the criterion. The 40 m spacing was selected as a compromise among safety, drainage performance, and construction cost. Although the 10 m case gives lower concentrations, it represents over-control and would require a denser borehole array and lie in the face-end disturbed zone. The 50 m case is excluded because its maximum concentration (1.0577%) exceeds 1.0%. At 40 m, the maximum concentration is 0.8659%, below the threshold, and the borehole CH_4 mass flow (0.2916 kg/s) and outlet CH_4 concentration (9.7009%) remain favorable. Therefore, 40 m is the largest tested spacing satisfying the safety constraint while minimizing borehole density, and is recommended as a balanced choice.

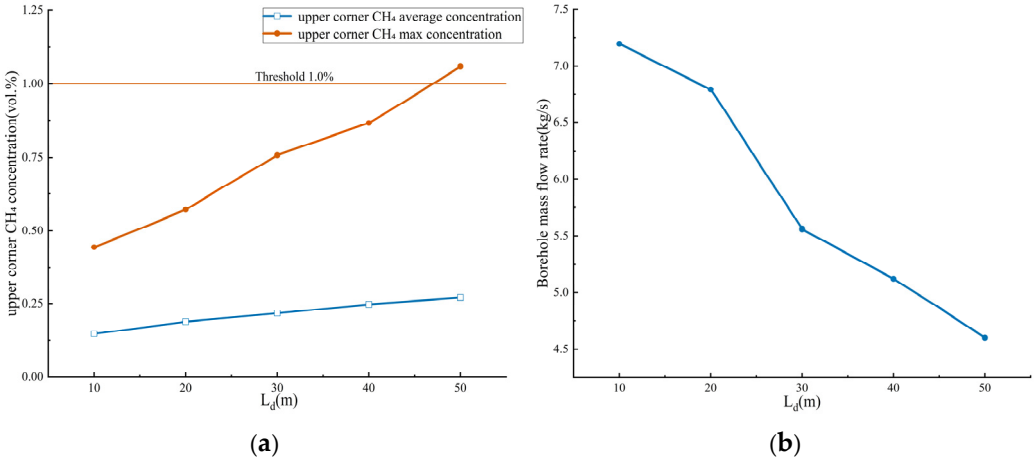


Figure 4. Effects of borehole-to-corner spacing on the reported steady-state performance metrics: (**a**) mean and maximum upper-corner methane (CH_4) concentrations; (**b**) total mixed-gas mass flow rate at the borehole outlet.

3.3. Methane Migration Mechanisms at the Selected Spacing

Velocity and CH_4 distributions before and after drainage at L_d = 40 m were compared to examine the control mechanism. The velocity vectors on the horizontal plane at y = 2 m before and after drainage are shown in Figure 5a,b, respectively. Positive direction denotes flow from the goaf toward the working face, and the summed positive-direction mass flow is the sum of positive face-normal fluxes over interface cells, rather than the net mass flow. At the goaf–working-face interface, the summed positive-direction mixed-gas mass flow from the goaf toward the working face was reduced from 9.4169 to 4.9188 kg/s, a reduction of 47.77%. At 40 m, the mixed-gas mass flow from the goaf into the borehole was approximately 5.1245 kg/s. These changes indicate that local gas flow was redistributed by drainage and that mixed-gas flow from the goaf toward the working face was reduced.

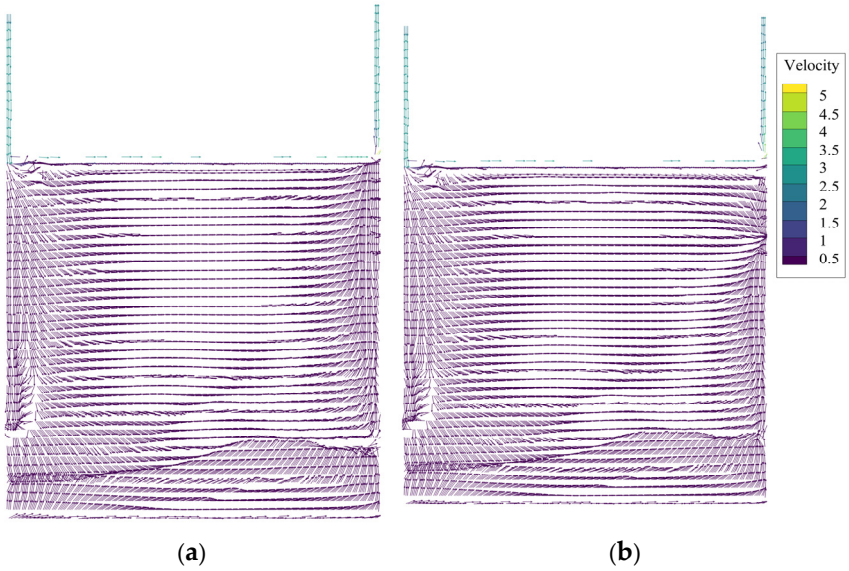
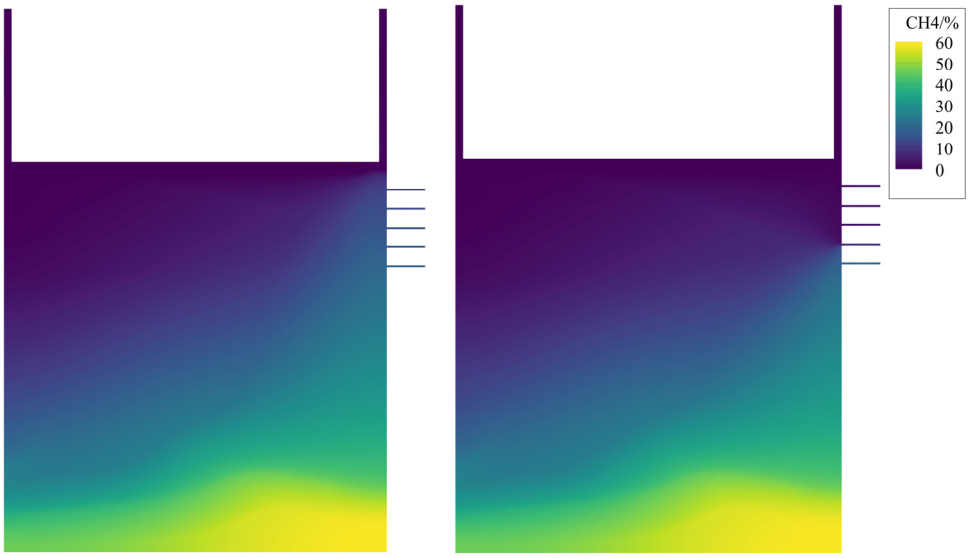


Figure 5. Flow fields before and after drainage at Ld = 40 m: (**a**) velocity vectors without drainage; (**b**) velocity vectors with drainage.

The CH_4 distributions at y = 2 m before and after drainage are shown in Figure 6a,b, respectively. On the upper-corner monitoring plane, the mean CH_4 concentration was

reduced from 1.2719% to 0.2475%, and the maximum was reduced from 2.1028% to 0.8659%. The respective reductions of 80.54% and 58.82% indicate lower mean concentrations and less local peak accumulation.



(**a**) (**b**)

Figure 6. Methane (CH_4) distributions before and after drainage: (**a**) CH_4 contours at y = 2 m without drainage; (**b**) CH_4 contours at y = 2 m for the 40 m case.

Upper-corner methane accumulation was reduced by composite-borehole drainage through lower inlet pressure, an additional gas outlet, and redistribution of local flow. Borehole spacing should be assessed using the local maximum upper-corner CH_4 concentration together with drainage performance metrics.

Drainage-induced changes in air leakage and oxygen transport have been examined in coupled studies of methane extraction and spontaneous-combustion zoning [30,31]. For surface boreholes in combustion-prone seams, field monitoring and simulations of coupled fields have linked methane removal to oxygen ingress and oxidation-zone response.

4. Composite Borehole Drilling and Field Performance

A suitable composite-borehole location was identified by the computational fluid dynamics (CFD) analysis in Section 3. Field trials were then conducted at working face 81506 of Huayang No. 2 Mine to assess drilling feasibility, the first 24 h of drainage, and performance over 60 days.

4.1. Coordinated Dual-Auger Drilling

The field drilling system comprised a drilling rig, dual-auger drill rods, and two 550 mm diameter drill bits. Two communicating circular holes were formed along the drilling direction by two parallel drill strings rotating in opposite directions. Both drill strings were advanced simultaneously. Coal was cut by the bits, and cuttings were removed by the auger flights. After the design depth was reached, the drill strings were withdrawn, the borehole was sealed, and the drainage pipeline was connected. The drilling equipment and resulting composite-borehole geometry are shown in Figure 7.

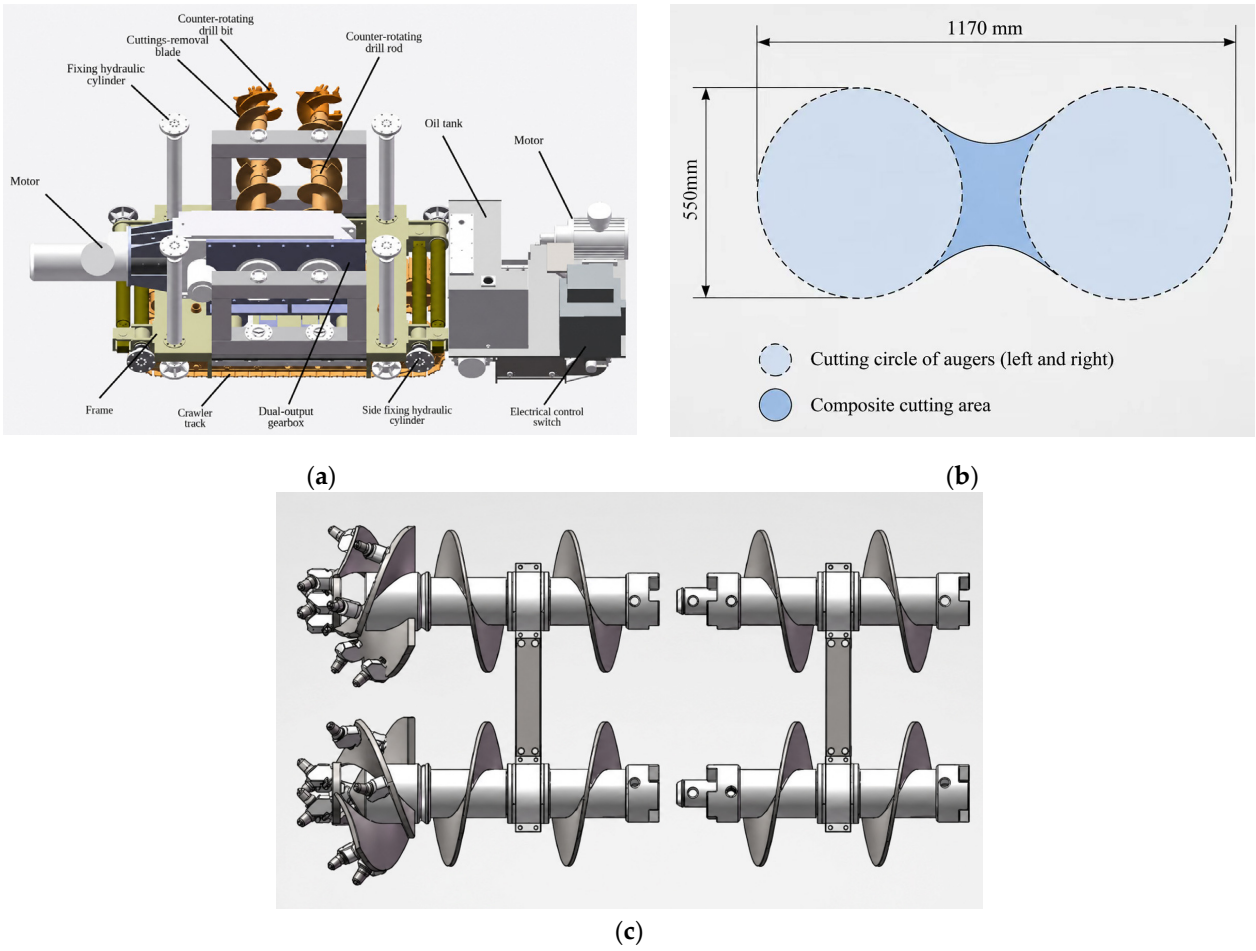


Figure 7. Coordinated dual-auger drilling equipment and composite-borehole geometry: (**a**) drilling equipment; (**b**) borehole cross-section; (**c**) dual-auger drill assembly.

4.2. Field Trial Design

The field trial was conducted at working face 81506 of Huayang No. 2 Mine. The approximately 3.50 m thick No. 8 coal seam was extracted at depths of 442–706 m, and U-type ventilation was used. Based on the placement analysis in Section 3, the composite borehole was installed 40 m from the upper corner. The borehole was 20 m deep, and the drainage gauge pressure was −1200 Pa. The borehole location at working face 81506 is shown in Figure 8.

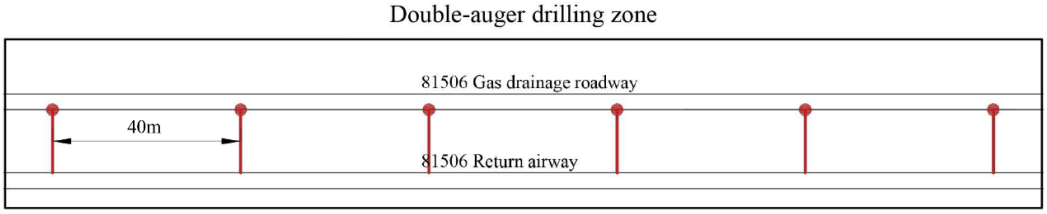


Figure 8. Composite-borehole location at working face 81506.

Conditions before and after borehole drainage were compared. The baseline was established from 14 days of continuous monitoring before drainage. Conditions were monitored continuously for 60 days after stable operation of the composite borehole had been established. Upper-corner CH_4 was measured by a mining methane sensor (0–4%, ±0.1%; Xuzhou Jiangmei Technology Co., Ltd., Xuzhou, China) installed near the return-air

side of the upper corner, about 0.2 m below the roof and 0.2 m from the side wall. Upper-corner CH_4 concentration, borehole outlet CH_4 concentration, and drainage pressure were measured. The field trial conditions and monitoring design are summarized in Table 5.

Table 5. Field trial and monitoring design.

Parameter	Before Drainage	After Drainage
Monitoring duration (d)	14	60
Average air volume of working face (m^3/min)	2385	2432
Borehole-upper corner distance (m)	—	40
Extraction pressure (Pa)	—	−1200
CH_4 sampling interval (min)	1	1
Upper corner CH_4 Sampling interval (min)	—	1

The mean was calculated as the arithmetic average of all valid 1 min records in each period, and the maximum as the highest 1 min value. The proportion of time above 1.0% was calculated as the ratio of 1 min records exceeding 1.0% to the total number of valid records.

4.3. Field Performance

4.3.1. First 24 h of Drainage

The first 24 h described in this section is the startup period, and the 60-day statistics in Section 4.3.2 refer to the subsequent stable-operation period and exclude this startup period. During startup, the 1 min records were aggregated into 24 hourly means. The upper-corner CH_4 concentration and mixed-gas flow rate are shown in Figure 9.

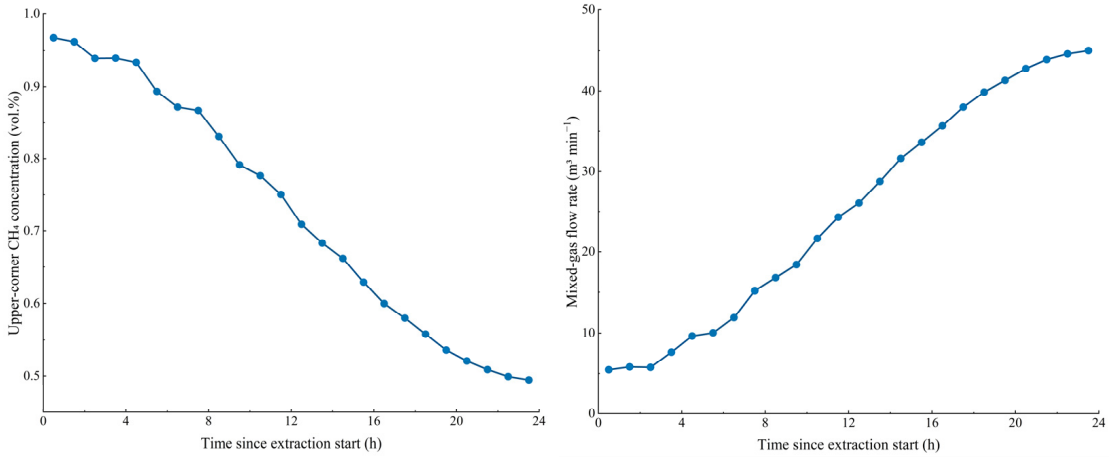


Figure 9. Drainage response during the first 24 h: (**a**) hourly mean upper-corner methane (CH_4) concentration; (**b**) hourly mean mixed-gas flow rate.

In hour 1, the upper-corner CH_4 concentration was 0.9674 vol.%, and the mixed-gas flow rate was 5.46 m^3/min. By hour 24, these values were 0.4945 vol.% and 45.02 m^3/min, respectively. The concentration decreased by 48.88%, while the flow rate increased to 8.25 times its initial value.

Between hours 20 and 24, the flow rate increased from 41.33 to 45.02 m^3/min, while the upper-corner CH_4 concentration decreased from 0.5359 to 0.4945 vol.%. The hourly changes became smaller, indicating that the response was slowing.

4.3.2. Upper-Corner Methane Control

Under the field conditions described above, upper-corner methane concentrations decreased after composite-borehole operation began. The mean upper-corner CH_4 concentration decreased from 1.08% before drainage to 0.557% during stable operation, a reduction of 48.43%. The maximum concentration decreased from 1.46% to 0.88%, a reduction of 39.73%. These decreases suggest that both overall methane concentrations and short-duration peaks in the upper corner were reduced during drainage.

Before drainage, upper-corner CH_4 concentrations were relatively high and fluctuated substantially. After drainage began, lower concentrations, reduced variability, and smaller short-duration peaks were observed. With 1.0% as the high-concentration threshold, the proportion of monitoring time above this value decreased from 64.3% before drainage to zero during stable operation. These observations indicate lower mean concentrations and fewer upper-corner methane exceedances.

Return-air CH_4 concentrations decreased in parallel with those in the upper corner. The mean return-air CH_4 concentration decreased from 0.97% before drainage to 0.366% during stable operation, a reduction of 62.27%. The upper-corner CH_4 concentration time series before and after drainage is shown in Figure 10a.

The simulation is not a quantitative validation of absolute concentrations: it omits overlying strata effects, dynamic mining-induced fractures, atmospheric pressure fluctuations, and operational variations, and evaluates concentrations on an area-weighted plane at $y = 2$ m from the stabilized transient state, whereas field data come from a fixed-point sensor over 60 days. The comparison therefore supports the relative trend and the maximum-concentration criterion rather than exact agreement.

The average air volume differed by only about 2.0% between the two periods, which is considered negligible relative to the observed concentration reductions.

4.3.3. Borehole Drainage Performance

At a drainage gauge pressure of −1.2 kPa, the mixed-gas flow rate was 44.09 m^3/min at standard conditions, and the borehole outlet CH_4 concentration was 33.31%. Standard conditions were 20 °C and 101.325 kPa, and the reported values are the mean of the 1 min records over the 60-day stable-operation period. The corresponding CH_4 volumetric flow rate was calculated as 14.69 m^3/min from the mixed-gas flow rate and outlet CH_4 volume fraction. These values indicate sustained drainage of methane-rich gas through the borehole.

Drainage throughput, methane content of the extracted gas, and methane removal rate are characterized by the mixed-gas flow rate, outlet CH_4 concentration, and CH_4 volumetric flow rate, respectively. Effective methane control cannot be established from a high mixed-gas flow rate alone. Because the CH_4 volumetric flow rate depends on both mixed-gas flow and outlet CH_4 volume fraction, these quantities should be considered together.

After startup, the mixed-gas flow rate, outlet CH_4 concentration, and CH_4 flow rate fluctuated initially and became relatively stable after approximately 24 h. Continuous operation was maintained throughout the 60-day monitoring period.

The mixed-gas flow rate and outlet CH_4 concentration over the 60-day monitoring period are shown in Figure 10b,c, respectively. Together with the upper-corner concentrations in Figure 10a, these data indicate that relatively low upper-corner methane levels coincided with stable borehole drainage.

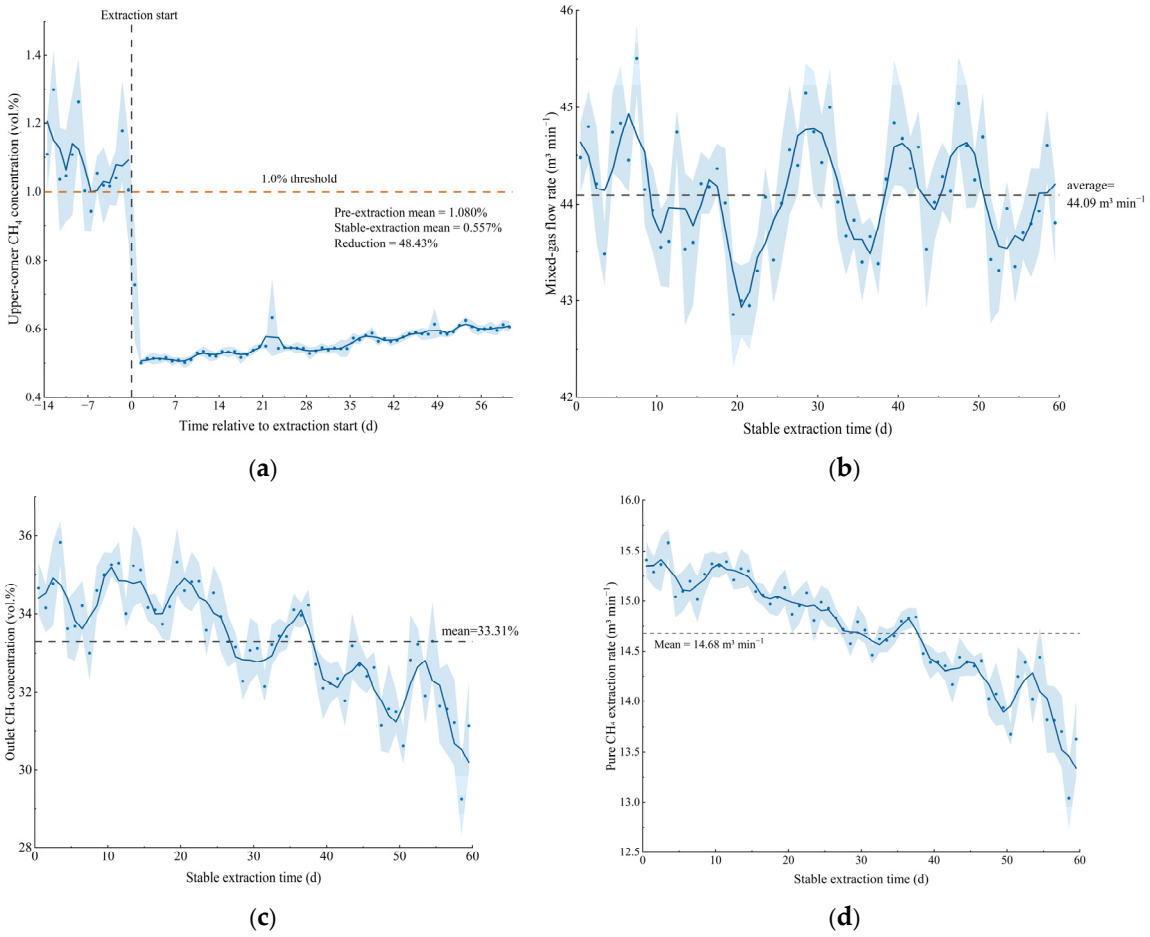


Figure 10. Upper-corner methane concentration and drainage parameters during borehole operation: (**a**) upper-corner methane (CH_4) concentration; (**b**) mixed-gas flow rate at standard conditions; (**c**) outlet CH_4 concentration; (**d**) CH_4 volumetric flow rate at the borehole outlet.

5. Discussion

Upper-corner methane accumulation was reduced by drainage through a dual-auger composite borehole, which provided an alternative outlet for methane-bearing gas. This continuous, large-cross-section borehole was formed in a single pass, increasing the drainage section per borehole and reducing the number of boreholes required for a given coverage. At 40 m, the simulated mixed-gas flow toward the working face decreased by 47.77%, supporting flow interception and redistribution through the heterogeneous goaf; the simulated mean and maximum CH_4 concentrations were 0.2475% and 0.8659%.

Among the five tested distances, 40 m was the largest satisfying the 1.0% maximum-concentration criterion, whereas 50 m exceeded it (1.0577%). It is therefore a recommendation for the investigated conditions rather than a universal optimum, reflecting a compromise among safety, drainage performance, and borehole cost. During the 60-day trial, mean and maximum upper-corner CH_4 concentrations decreased by 48.43% and 39.73%, to 0.557% and 0.88%, and the time above 1.0% fell from 64.3% to zero.

In summary, at the selected 40 m spacing, the simulated mean and maximum upper-corner CH_4 concentrations were 0.2475% and 0.8659%, and the mixed-gas flow toward the working face decreased by 47.77%; in the field, the mean and maximum concentrations decreased by 48.43% and 39.73%, to 0.557% and 0.88%, with the time above 1.0% falling from 64.3% to zero. The 40 m recommendation is conditional on the model assumptions,

the reported emission rate of 0.2616 kg/s, the ventilation and suction conditions, and the 1.0% criterion, and broader applicability requires site-specific verification.

6. Conclusions

Under the tested conditions, dual-auger composite borehole drainage provided a feasible approach to upper-corner methane control. The combined numerical assessment and field monitoring offer a basis for site-specific borehole placement, with local calibration and continued monitoring required for application to other working faces.

Author Contributions: Conceptualization, Z.C.; Methodology, Z.C., X.Z. and X.Q.; Formal Analysis, Z.C.; Investigation, L.Z., X.L., J.S. and W.L.; Writing—Original Draft, Z.C.; Writing—Review & Editing, X.Z. and X.Q.; Visualization, Z.C.; Supervision, X.Z. and X.Q.; Project Administration, X.L.; Funding Acquisition, X.L. All authors have read and agreed to the published version of the manuscript.

Funding: This research was funded by the National Natural Science Foundation of China (General Program), grant number 52474244, and the Shanxi Key Laboratory of Life Rescue Access Construction Technology and Equipment for Confined Space Emergency Response, grant number 202504010931039.

Data Availability Statement: The data generated and analyzed during the current study are available from the corresponding author on reasonable request.

Acknowledgments: The authors thank Huayang No. 2 Mine for providing the site for the field trials.

Conflicts of Interest: The authors declare no conflicts of interest.

References

1. Fan, C.; Xu, H.; Wang, G.; Wang, J.; Liu, Z.; Cheng, Q. Determination of roof horizontal long drilling hole layout layer by dynamic porosity evolution law of coal and rock. *Powder Technol.* **2021**, *394*, 970–985. [CrossRef]
2. Shang, Y.; Zhang, L.; Kong, D.; Wang, Y.; Cheng, Z. Overlying strata failure mechanism and gas migration law in close distance outburst coal seams: A case study. *Eng. Fail. Anal.* **2023**, *148*, 107214. [CrossRef]
3. Feng, G.; Li, Z.; Hu, S.; Zhang, Y.; Zhang, A.; Gao, Q.; Jiang, H.; Guo, X.; Li, C.; Cui, J. Distribution of gob empty space for methane drainage during the longwall mining: A case study. *J. Nat. Gas Sci. Eng.* **2018**, *60*, 112–124. [CrossRef]
4. Juganda, A.; Strebinger, C.; Brune, J.F.; Bogin, G.E. Discrete modeling of a longwall coal mine gob for CFD simulation. *Int. J. Min. Sci. Technol.* **2020**, *30*, 463–469. [CrossRef]
5. Wang, Y.; Si, G.; Xiang, Z.; Oh, J.; Belle, B.; Webb, D. A theoretical goaf resistance model based on gas production analysis in goaf gas drainage. *Int. J. Coal Geol.* **2022**, *264*, 104140. [CrossRef]
6. Liu, S.; Shi, G.; Ren, H.; Wang, D. Effect of diurnal fluctuation of atmospheric pressure on gas migration in goaf of coal mine. *Process Saf. Environ. Prot.* **2023**, *174*, 310–319. [CrossRef]
7. Lolon, S.A.; Brune, J.F.; Bogin, G.E., Jr.; Grubb, J.W.; Saki, S.A.; Juganda, A. Computational fluid dynamics simulation on the longwall gob breathing. *Int. J. Min. Sci. Technol.* **2017**, *27*, 185–189. [CrossRef]
8. Duda, A. The Impact of Atmospheric Pressure Changes on Methane Emission from Goafs to Coal Mine Workings. *Energies* **2024**, *17*, 173. [CrossRef]
9. Liu, C. Optimizing Methane Control in Composite Goaf Areas: Insights from Multisource Emission Analysis and Numerical Modeling in the Tongxin Coal Mine. *ACS Omega* **2024**, *9*, 41171–41178. [CrossRef]
10. Hasheminasab, F.; Bagherpour, R.; Aminossadati, S.M. Numerical simulation of methane distribution in development zones of underground coal mines equipped with auxiliary ventilation. *Tunn. Undergr. Space Technol.* **2019**, *89*, 68–77. [CrossRef]
11. Sadeghi, S.; Aminossadati, S.M.; Kizil, M.; Leonardi, C. Computational Investigation of shearer movement and drum rotation effects on airflow and methane dispersion in longwalls using integrated dynamic and overset meshing. *Tunn. Undergr. Space Technol.* **2025**, *161*, 106500. [CrossRef]
12. Xu, C.; Wang, K.; Li, X.; Yuan, L.; Zhao, C.; Guo, H. Collaborative gas drainage technology of high and low level roadways in highly-gassy coal seam mining. *Fuel* **2022**, *323*, 124325. [CrossRef]
13. Zhou, A.; Xu, Z.; Wang, K.; Wang, Y.; An, J.; Shi, Z. Coal mine gas migration model establishment and gas extraction technology field application research. *Fuel* **2023**, *349*, 128650. [CrossRef]
14. Jia, H.; Wang, Z.; Zhao, X.; Ma, S.; Song, Z.; Chen, J. Characterization of spatiotemporal distribution of gas in the goaf of W-type ventilated working face. *Process Saf. Environ. Prot.* **2024**, *184*, 1379–1388. [CrossRef]

15. Leśniak, G.; Brunner, D.J.; Topór, T.; Słota-Valim, M.; Cicha-Szot, R.; Jura, B.; Skiba, J.; Przystolik, A.; Lyddall, B.; Plonka, G. Application of long-reach directional drilling boreholes for gas drainage of adjacent seams in coal mines with severe geological conditions. *Int. J. Coal Sci. Technol.* **2022**, *9*, 88. Correction in *Int. J. Coal Sci. Technol.* **2023**, *10*, 39. [CrossRef]
16. Jia, L.; Peng, S.; Xu, J.; Yan, F.; Chen, J.; Wu, B. Investigation on gas drainage effect under different borehole layout via 3D monitoring of gas pressure. *J. Nat. Gas Sci. Eng.* **2022**, *101*, 104522. [CrossRef]
17. Lin, J.; Ren, T.; Wang, G.; Booth, P.; Cheng, Y.; Black, D.; Hungerford, F.; Nemcik, J. Field trials of nitrogen injection enhanced gas drainage in hard-to-drain coal seam by using underground in-seam (UIS) boreholes. *Fuel* **2022**, *328*, 125293. [CrossRef]
18. Miao, D.; Chen, X.; Ji, J.; Lv, Y.; Zhang, Y.; Sui, X. New Technology for Preventing and Controlling Air Leakage in Goaf Based on the Theory of Wind Flow Boundary Layer. *Processes* **2022**, *10*, 954. [CrossRef]
19. Aghighi, M.A.; Lv, A.; Siddiqui, M.A.Q.; Masoumi, H.; Thomas, R.; Roshan, H. A multiphysics field-scale investigation of gas pre-drainage in sorptive sediments. *Int. J. Coal Geol.* **2022**, *261*, 104098. [CrossRef]
20. Wang, W.; Li, Z.; Yu, H. Goaf Gas Control Improvement by Optimizing the Adjacent Roadway Large-Diameter Boreholes. *Adv. Civ. Eng.* **2021**, *2021*, 1933010. [CrossRef]
21. Zhang, L.; Ge, Z.; Lu, Y.; Zhou, Z.; Xiao, S.; Deng, K. Tree-Type Boreholes in Coal Mines for Enhancing Permeability and Methane Drainage: Theory and an Industrial-Scale Field Trial. *Nat. Resour. Res.* **2020**, *29*, 3197–3213. [CrossRef]
22. Zhao, W.; Wang, K.; Zhang, R.; Dong, H.; Lou, Z.; An, F. Influence of combination forms of intact sub-layer and tectonically deformed sub-layer of coal on the gas drainage performance of boreholes: A numerical study. *Int. J. Coal Sci. Technol.* **2020**, *7*, 571–580. [CrossRef]
23. Cai, J.; Wu, J.; Yuan, S.; Liu, Z.; Kong, D. Numerical analysis of multi-factors effects on the leakage and gas diffusion of gas drainage pipeline in underground coal mines. *Process Saf. Environ. Prot.* **2021**, *151*, 166–181. [CrossRef]
24. Lei, Y. Movement Law of Methane Drained by Large-Diameter Borehole Drilling Machine in the Goaf. *Processes* **2022**, *10*, 1669. [CrossRef]
25. Guo, M.; Guo, W.; Yuan, R.; Tan, Y.; Bai, E. Study on the effective drainage range of long horizontal borehole for goaf gas drainage. *Energy Sci. Eng.* **2024**, *12*, 4323–4334. [CrossRef]
26. Li, X.; Guo, S.; Mu, B. Numerical simulation of gas drainage from goaf via high-level borehole in gently inclined seams. *AIP Adv.* **2025**, *15*, 035037. [CrossRef]
27. Xu, P.; Yang, W.; Li, S.; Shuang, H.; Zhang, X.; Chen, X.; Guo, C. Extraction Technology of Pressure-Relief Gas Based on the Co-Evolution and Zoning Mechanism of Mining-Induced Overburden Fracture. *Appl. Sci.* **2026**, *16*, 6677. [CrossRef]
28. Ma, Q.; Xue, J.; Shi, Y.; Zeng, X. Characteristics of Porosity Distribution and Gas Migration in Different Layers of Comprehensive Working Face Goaf. *Energies* **2023**, *16*, 2325. [CrossRef]
29. Lv, X.; Hu, S.; Nian, J.; Deng, C.; Zhao, B.; He, C.; Wang, Y.; Zhang, X.; Zhang, W. Gas migration control in goaf with double roof cutting and retaining roadway. *Sci. Rep.* **2024**, *14*, 29743. [CrossRef]
30. Wang, J.; Zhang, S.; Yang, X.; Huang, Y.; Hao, C.; Chen, L. Coupled Mechanism of Goaf Gas Drainage and Spontaneous-Combustion Three-Zone Evolution in a Longwall Working Face: A Case Study. *Processes* **2026**, *14*, 2116. [CrossRef]
31. Liu, S.; Yang, Y.; Wu, L.; Zhai, Y.; Yang, W.; Li, L.; Lei, J. Coupled thermal–oxygen–methane field evolution and coordinated prevention strategy in goaf under surface borehole drainage. *Process Saf. Environ. Prot.* **2025**, *203*, 107897. [CrossRef]

Disclaimer/Publisher's Note: The statements, opinions and data contained in all publications are solely those of the individual author(s) and contributor(s) and not of MDPI and/or the editor(s). MDPI and/or the editor(s) disclaim responsibility for any injury to people or property resulting from any ideas, methods, instructions or products referred to in the content.